Supplementary Information (SI) for Journal of Materials Chemistry A.
This journal is © The Royal Society of Chemistry 2026

Supporting information

Molecular Fusion in Covalent Organic Frameworks Promotes Oxygen Reduction and Water Oxidation for Efficient Photocatalytic H_2O_2 Production

Lin Wang,[a†] Hang Chi,[b†] Peng Han,[a] Qiuyan Ma,[a] Jia-Xing Jiang,[c*] Shiyong Gao,[a] Yong Zhang[a,d*]

[a] School of Materials Science and Engineering, Harbin Institute of Technology, Harbin 150001, China

[b] The Second Affiliated Hospital of Harbin Medical University, Harbin 150086, China

[c] Key Laboratory of Optoelectronic Chemical Materials and Devices (Ministry of Education), School of Optoelectronic Materials & Technology, Jianghan University, Wuhan 430056, China.

[d] Zhengzhou Research Institute, Harbin Institute of Technology, Zhengzhou 450007, China

Corresponding author: yongzhang@hit.edu.cn (Y. Zhang), jiaxing@jhun.edu.cn (J-X Jiang)

† These authors contributed equally.

Experimental Section:

Materials: All reagents and solvents were used as received from commercial sources unless otherwise noted. 1,3,5-Trichlorobenzene (99%), aluminium chloride ($AlCl_3$, 99%), p-dithiane-2,5-diol (98%), 4,4',4''-(1,3,5-Triazine-2,4,6-triyl)trianiline (99%), 5,5',5''-(Benzene-1,3,5-triyl)tris(thiophene-2-carbaldehyde) (99%), o-dichlorobenzene (o-DCB), ethanol (EtOH), 1,3,5-Trimethylbenzene, 1,4-Dioxane and n-butanol (n-BnOH) were purchased from Anhui Zesheng Technology Co., Ltd. t Anhui, China. toluene was purchased from China National Pharmaceutical Group Co., Ltd, Beijing, China. All the commercial chemicals were directly used without further purification. Solvents were purified according to standard procedures.

Material synthesis:

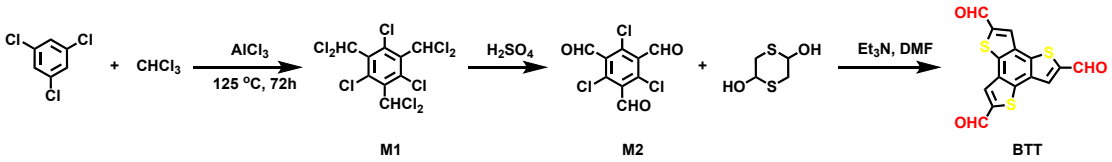

Scheme S1. Synthesis of BTT.

The synthesis of BTT is strictly based on published papers.[1]

Synthesis of M1: 1,3,5- trichlorobenzene (6 g, 33.2 mmol), $AlCl_3$ (5.2 g, 39.2 mmol), and $CHCl_3$ (80 mL) were added to a teflon-lined stainless-steel autoclave (150 mL) and heated at 125 °C for 72 h. At 6 h and 18 h after the start of the reaction, the autoclave was cooled to room temperature and opened to relieve the pressure. After 72h, the reaction was cooled to room temperature, 120 mL of $CHCl_3$ was added, and all the reaction mixture was poured into a concentrated hydrochloric acid/ice mixture and stirred for 1h. The separated organic layer was washed with $NaHCO_3$ and brine, and dried with $MgSO_4$. After concentration and purification by column chromatography to get M1 (9.7 g, 68%).

Synthesis of M2. Add M1 (2.5 g, 5.8 mmol) together with 18 ml of H_2SO_4 to 250 ml three-neck round-bottom flask and stir at 40°C for 1 h. Then, dissolve $NaHCO_3$ (20 g, 0.24 mmol) in ice water and slowly add it to the three-neck round-bottom flask under ice bath conditions, maintaining the reaction temperature below 5°C during the reaction. The formed precipitate was filtered off, wash with water, and purify by column chromatography to obtain the yellow product M2 (0.81 g, 52%).

Synthesis of BTT. M2 (2 g, 7.53 mmol) and p-dithiane-2,5-diol (1.72 g, 11.3 mmol) were dispersed into 40 ml DMF in a three-necked flask at room temperature, then triethylamine (6.28 ml, 45.2 mmol) was added, and the reaction system was heated at 35°C with stirring for 8 h. Then, the reaction mixture was poured into ice water, the precipitate was centrifuged and washed constantly with water and THF, yielding dark yellow BTT (1.81 g, 72.7%).

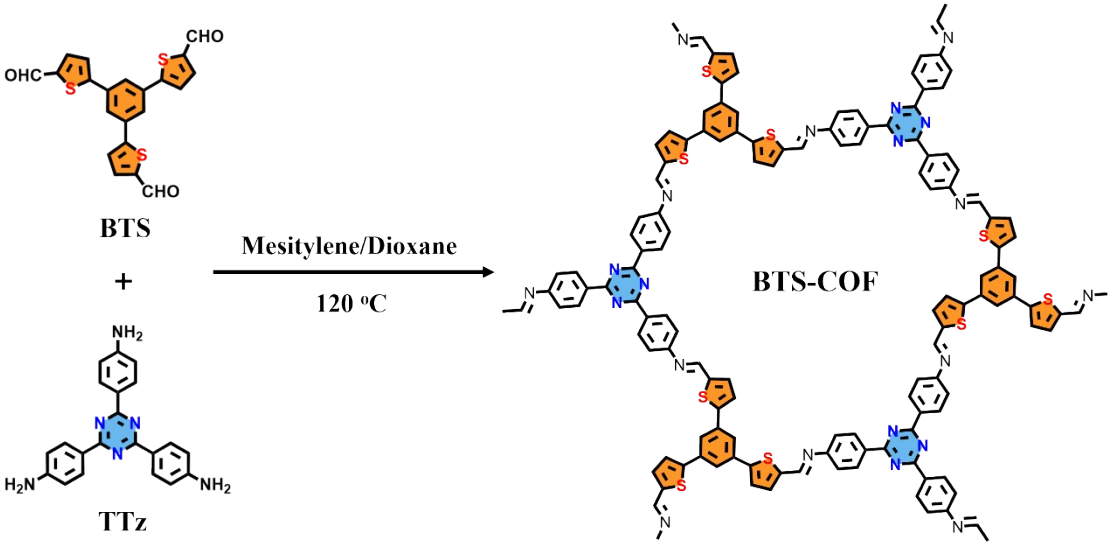

Scheme S2. Synthesis of BTS-COF.

Synthesis of BTS-COF. The BTS-COF was synthesized by solvothermal condensation reaction. 5,5',5"-(Benzene-1,3,5-triyl)tris(thiophene-2-carbaldehyde) (BTS) (41 mg, 0.1mmol) and 4,4',4"-(1,3,5-Triazine-2,4,6-triyl)trianiline (TTz) (35.4 mg, 0.1 mmol) were dissolved in a mixed solvent of 1 mL mesitylene, 1 mL dioxane and 0.2 mL 6M aqueous acetic acid in a pyrex tube. This mixture was sonicated for 10 min to get a homogeneous dispersion. Then, the pyrex tube was flash frozen in a liquid N_2 bath and degassed by freeze-pump-thaw technique for three times and sealed under vacuum. Upon warming to room temperature, the tube was placed in an oven and heated at 120 °C for 72 h. The precipitate was collected by filtration, washed with DMF (8 × 5 mL), extracted by Soxhlet extractor with tetrahydrofuran for 24 hours, and finally dried at 60 °C under vacuum for 12 hours to obtain yellow crystalline powder. Yield: 76.8%.

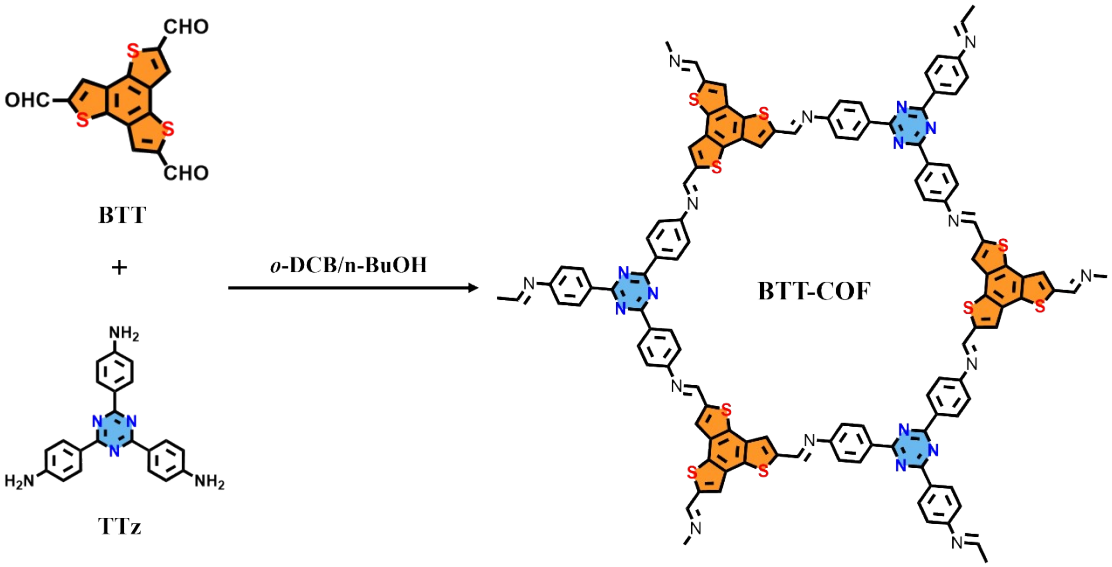

Scheme S3. Synthesis of BTT-COF.

Synthesis of BTT-COF. The BTT-COF was synthesized by solvothermal condensation reaction.

BTT (33.4 mg, 0.1 mmol) and TTz (35.4 mg, 0.1 mmol) were dissolved in a mixed solvent of 1 mL o-DCB, 1 mL n-BuOH and 0.2 mL 6M aqueous acetic acid in a pyrex tube. This mixture was sonicated for 10 min to get a homogeneous dispersion. Then, the pyrex tube was flash frozen in a liquid N_2 bath and degassed by freeze-pump-thaw technique for three times and sealed under vacuum. Upon warming to room temperature, the tube was placed in an oven and heated at 120 °C for 72 h. The precipitate was collected by filtration, washed with DMF (8 × 5 mL), extracted by Soxhlet extractor with tetrahydrofuran for 24 hours, and finally dried at 60 °C under vacuum for 12 h to obtain yellow crystalline powder. Yield: 81.5%.

General characterization: Liquid ^{1}H NMR spectra were measured using a 400 MHz Bruker Avance spectrometer. Solid-state 13C CP-MAS NMR measurements were conducted on 400 MHz Bruker Avance III solid state NMR spectrometer equipped with a standard 4 mm MAS double resonance probe head. Fourier transform infrared (FT-IR) spectra were collected using a Bruker Vertex 70 FTIR spectrometer in the attenuated total reflection (ATR) mode. XRD was performed on a PANalytical X-ray diffractometer with monochromatic Cu Kα radiation. Single crystal XRD was carried out on Agilent Gemini Atlas X-ray diffractometer at 223 K with a graph itemonochromated Cu Kα radiation source (λ = 1.54184 Å). XPS results were obtained on an Ultra DLD X-ray photoelectron spectrometer. SEM images were taken on a Supera 55 Zeiss scanning electron microscope. TEM imaging was carried out on an FEI Talos F200X transmission electron microscope operating at 200 kV. Barret-Emmett-Teller (BET) surface areas were measured from N_2 adsorption and desorption on a Micromeritics ASAP 2020 HD88 analyzer at 77 K and the pore size

distribution was calculated based on the N_2 sorption isotherm by using Density Functional Theory (DFT, a carbon model containing slit/cylindrical pore) model at 3FLEX software. Solid-state UV-Vis diffuse reflectance spectra were measured on a Perkin Elmer Lambda 950 spectrophotometer. Time-resolved PL lifetime measurements were conducted with a FluoroHub single photon counting controller. EPR analyses were conducted on a Bruker A300 spectrometer under visible light irradiation (λ>420 nm) at room temperature. TGA was conducted on a Mettler Toledo TGA thermal analyzer under N_2 with the temperature ramping from 25 ^{o}C to 800 ^{o}C at a rate of 10 ^{o}C/min. Kelvin probe atomic force microscopy (KPAFM) was used to characterize the surface voltages of BTS-COF and BTT-COF with a resolution of 512 dots per line at 1 Hz. a probe (AC 160) was used for the measurements. BTS-COF and BTT-COF were dispersed in ethanol, dripped onto the wafers, and dried well under an infrared heat lamp before measurement. processing of the KPAFM images was performed with the help of Nanoscope Analysis. Transient absorption (TA) spectroscopy was carried out by using an optical instrument combined with a frequency-doubled mode-locked Ti: sapphire femtosecond laser (coherent) and an optical parametric amplifier (OPA) system. The

amplified Ti: sapphire femtosecond laser generates seed pulses with a 35 fs pulse width and a repetition rate of 1 kHz. The seed pulses are divided into two distinct beams. The strong beam is sent to the OPA system and provided the 400 nm pump laser pulse, and the other one is focused onto a sapphire crystal to generate a white light continuum, providing a broad band of 430-750 nm UV-vis probe light. The excitation beam has a low energy of 0.1 μJ per pulse to avoid the exciton-exciton and exciton-charge annihilation effects. The samples were sandwiched between two quartz glasses, which were filled with nitrogen, under continuous stirring. In situ diffuse reflectance infrared Fourier transfer (DRIFT) spectroscopy was performed using a Thermo Scientific Nicolet iS50 FT-IR spectrometer equipped with an in situ diffuse reflectance cell (Harrick). The photocatalyst was put inside the reaction cell consisting of a sample cup and a cover dome. The photocatalyst powder was pretreated with a stream of Ar for 10 min (10 mL min^{-1}) during the measurement. Water vapour was introduced into the reaction cell via an oxygen stream (25 mL min^{-1}) for 10 min. After reaching vapour adsorption equilibrium, the photocatalysts were irradiated with a xenon lamp and infrared spectra were collected every 10 min. The water contact angle was measured on a Krüss DSA100 Droplet Shape Analyser. The solid surface was checked on a catalyst analyser (Microtrac BELCAT II) for Oxygen-Temperature-Programmed Desorption measurements (O_2-TPD).

Photoelectrochemical measurements: A three-electrode cell was employed to measure the photocurrent on a CHI660E (Chenhua, Shanghai) electrochemical workstation. The working electrode was prepared by coating the mixture slurry of the polymer catalyst. 5% Nafion solution and ethanol as the binder on ITO, where the coating area was 1 cm^2. The working electrode was dried at 50°C for 0.5 hours before the measurement. A platinum plate and a Ag/AgCl electrode were used as the counter electrode and reference electrode, respectively and 0.5 M sodium sulfate solution was used as the electrolyte. A 300 W Xenon lamp was applied to illuminate the sample. The photocurrent measurements were conducted by directly irradiating the working electrode from the back side using a 300W xenon lamp equipped with a 420 nm cut-off filter. The rotating disc electrode test (RDE) uses a rotating disc electrode as a substrate for the working electrode. 2 mg of catalyst was dispersed in a mixture containing 0.5 mL of ethanol and 20 μL of Nafion solution (5 wt%) and then ultrasonicated to form a homogeneous catalyst suspension. The catalyst suspension (50 μL) was placed on a disc electrode and dried at room temperature. RDE measurements were carried out on a CHI760E workstation (CH Instruments, Co. Ltd.) using a RRDE-3A rotator (ALS Co., Ltd.) The Pt wire and Ag/AgCl electrode were used as counter electrode and reference electrode, respectively. Linear scanning voltammograms (LSV) were obtained at room temperature in O_2-saturated 0.1 M phosphate buffer solution (PBS, pH = 7.2) solution at a scan rate of 10 mV s^{-1} and different rotational speeds. For OER tests, voltammograms were obtained at room

temperature in N_2-saturated 0.1 M PBS at a scan rate of 10 mV s^{-1} and a rotational rate of 1600 rpm. The potential of the ring electrode was set to -0.23 V (vs. Ag/AgCl) to detect O_2. The potential of the ring electrode was set to +0.60 V (vs. Ag/AgCl) to detect H_2O_2.

Photocatalytic H_2O_2 production:

The H_2O_2 concentration was measured by a traditional cerium sulfate $Ce(SO_4)_2$ titration method based on the mechanism that a yellow solution of Ce^{4+} can be reduced by H_2O_2 to colourless Ce^{3+}. Thus, the concentration of Ce^{4+} before and after the reaction can be measured via the UV-vis spectrophotometer. The absorption peak used for the measurement was 316 nm.

$$2Ce^{4+} + H_2O_2 \rightarrow 2Ce^{3+} + 2H^+ + O_2$$

The yellow transparent $Ce(SO_4)_2$ solution (1 mM) was prepared by dissolving 33.2 mg $Ce(SO_4)_2$ in 100 mL 0.5 M sulfuric acid solution. To obtain the calibration curve, H_2O_2 with known concentration was added to $Ce(SO_4)_2$ solution and measured by a UV-vis spectrophotometer. Based on the linear relationship between the signal intensity and Ce^{4+} concentration, the H_2O_2 concentrations of the samples could be obtained.

5 mg of photocatalyst was dispersed in a mixed solution containing 50 mL pure water. The suspension was well dispersed by ultrasonication for 30 min and O_2 was bubbled into the suspension in the whole process of photocatalysis. A 300 W Xe lamp (CEL-HXF300 CEAULIGHT) with 420 nm cutoff filter was used as the light source during the measurement. 1 mL liquid was filtrated with a 0.22 μm filter to remove the photocatalysts. The sample was mixed with 300 μL pre-prepared $Ce(SO_4)_2$ solution and the concentrations of H_2O_2 was determined by the UV-vis spectrometer.

When reaction conditions interfere with the Ce^{4+} titration method, the typical iodine titration method is also used. Specifically, potassium iodide (KI) solution (0.4 mol L^{-1}, 1 mL) and potassium hydrogen phthalate ($C_8H_5O_4K$) solution (0.1 mol L^{-1}, 1 mL) are added to the sample solution (1 mL), and 1 mL of pure water is added to dilute the solution. The mixture is allowed to stand for 30 minutes before UV-VIS measurement. The reaction proceeds as follows:

$$H_2O_2 + 3I^- + 2H^+ \rightarrow 2H_2O + I_3^-$$

Among them, $C_8H_5O_4K$ is used as an indicator, measured by UV-VIS spectroscopy, and I_3^- has strong absorption at 350 nm.

Computational method: Molecular structures were optimized by B3LYP with the 6-31G(d) basis set (*J. Chem. Theory Comput. 2008, 4, 297-306*). The TD-DFT/CAM-B3LYP was utilized to obtain electrostatic potential since the function of CAM-B3LYP (19% HFexc at short-range and 65% HFexc at long-range) was able to take into account the effect of charge transfer (*Chem. Phys. Lett. 2004, 393, 51-57*). Inter-fragment charge transfer (IFCT) and distance of charge transfer (D_{CT}) were calculated using the Multiwfn 3.7 package (*J. Comput. Chem. 2012, 33, 580-592*) to understand intramolecular electron transition. All the calculations were performed using Gaussian

09 software package (Gaussian 09, Revision D.01. Wallingford, CT: Gaussian Inc (2013)). VMD software was used to display the calculation results (*J. Mol. Graph. 1996, 14, 33-38*).

All the DFT calculations were conducted based on the Vienna Ab-inito Simulation Package (VASP). The exchange-correlation effects were described by the Perdew-Burke-Ernzerhof (PBE) functional within the generalized gradient approximation (GGA) method. The core-valence interactions were accounted by the projected augmented wave (PAW) method. The energy cutoff for plane wave expansions was set to 400 eV, and the 3×3×1 Monkhorst-Pack grid k-points were selected to sample the Brillouin zone integration. The structural optimization was completed for energy and force convergence set at 1.0×10^{-4} eV and 0.05 eV $Å^{-1}$, respectively.The adsorption energy (E_{ads}) of O_2 is calculated by

$$Eads = E^*O_2 – EO_2 – E_{sub}$$

where E^*O_2 represents the energy after the adsorption of O_2 on the substrates. EO_2 is the energy of the O_2 molecule. E_{sub} is the energy of BTS-COF and BTT-COF.The Gibbs free energy change (ΔG) of each step is calculated using the following formula:

$$\Delta G = \Delta E + \Delta ZPE - T\Delta S$$

where ΔE is the electronic energy difference directly obtained from DFT calculations, ΔZPE is the zero-point energy difference, T is the room temperature (298.15 K) and ΔS is the entropy change. ZPE could be obtained after frequency calculation by:

$$ZPE = \frac{1}{2}\sum hvi$$

In Vitro Antibacterial Activity Analysis. The bacterial dispersion was diluted to 10^5 CFU/mL with phosphate buffer solution (PBS, pH 7.4), and then 500 μL of the diluted bacterial suspension was taken and mixed with 500 μL of the different material solutions, and xenon lamp (CEL-HXF300 CEAULIGHT, 150 mW/cm^2) illumination was applied for 10 min. After that, 10 μL of diluted bacterial suspension was taken and spread on solid medium and incubated at 37°C for 24 hours. Finally the number of colonies was counted. Each experiment was performed three times in parallel. The bacterial survival rate was calculated according to the following equation:

$$\text{Bacteria survival rate (\%)} = Ns/Nc \times 100\%$$

Where N_C and N_S, are the number of colonies in the control and sample groups.

In Vitro Live/Dead Bacterial Cell Staining. Taking 500 μl of each set of treated bacterial suspension and mixing it with SYTO-9/PI double staining kit for 30 min in the dark. During this process, live bacterial cells were stained with green fluorescence by SYTO-9 and dead bacterial cells were stained with red fluorescence by PI. The resulting bacterial samples were placed on the surface of glass slides and observed with a fluorescence microscope.

Morphological Characterization of Bacteria. Each group of treated bacterial suspensions was collected by centrifugation at 3000 rpm for 3 min and washed twice with PBS buffer, followed by

fixation in centrifuge tubes containing 2.5% glutaraldehyde solution for 12 h. After that, wash samples three times in PBS (pH 7.4), dehydrating with the sequential treatment of ethanol-water mixtures (30, 50, 70, 85, 90, 95, and 100%) for 10 min in each mixing ratio at room temperature, respectively. Finally, dried bacteria were sputter-coated with gold. The morphology analysis of the bacteria was characterized by SEM.

Anti-Bacterial Biofilm Activity Assay. 1 mL of bacterial suspension (10^6 CFU/mL) was added to a 24-well plate and incubated at 37°C for 48 hours to form mature biofilms. Mature biofilms were washed with PBS and subjected to different groups of materials. After that, they were washed three times with PBS, then incubated with anhydrous methanol for 10 min, and finally stained with 500 μL of 0.1% crystal violet for 10 min. The stained biofilms were washed three times with PBS. When the stained biofilm was dissolved in 500 μL of 95% ethanol, its absorbance at 590 nm was detected. Meanwhile, different treated biofilms were stained with SYTO-9 and PI for 20 min at 4°C, and then imaged by confocal laser scanning microscopy to obtain the three-dimensional structure of the biofilm.

Supplementary figures and tables

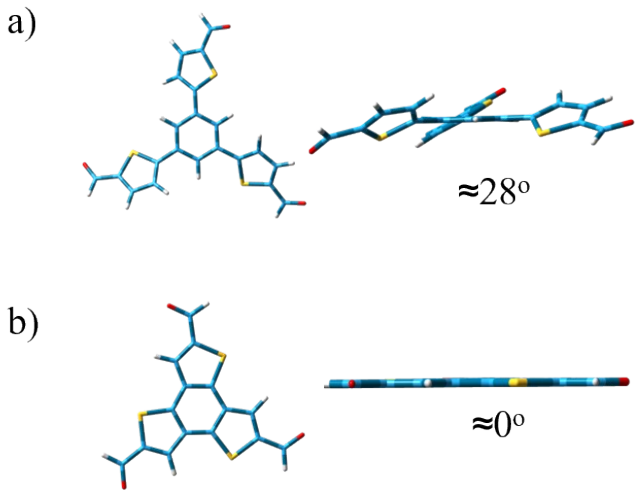

Fig. S1. Theoretical torsion angle of monomer molecules. a) BTS. b) BTT.

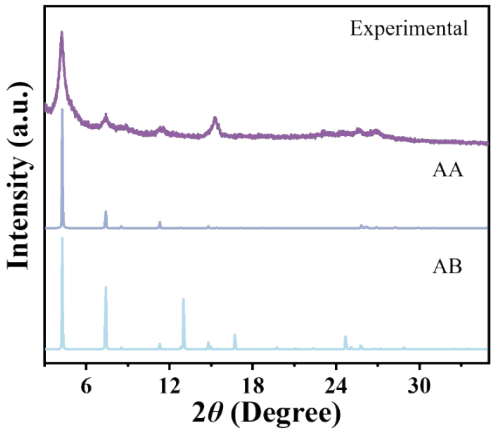

Fig. S2. Simulated PXRD spectra of BTS-COF under different stacking modes.

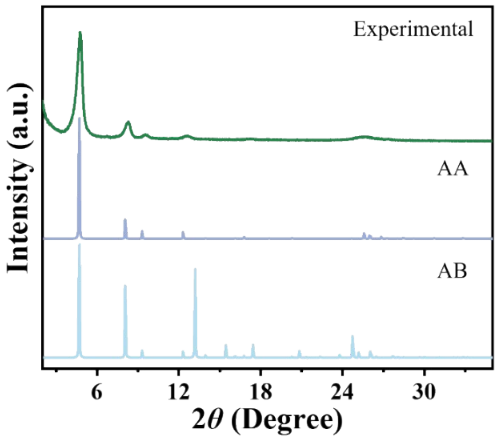

Fig. S3. Simulated PXRD spectra of BTT-COF under different stacking modes.

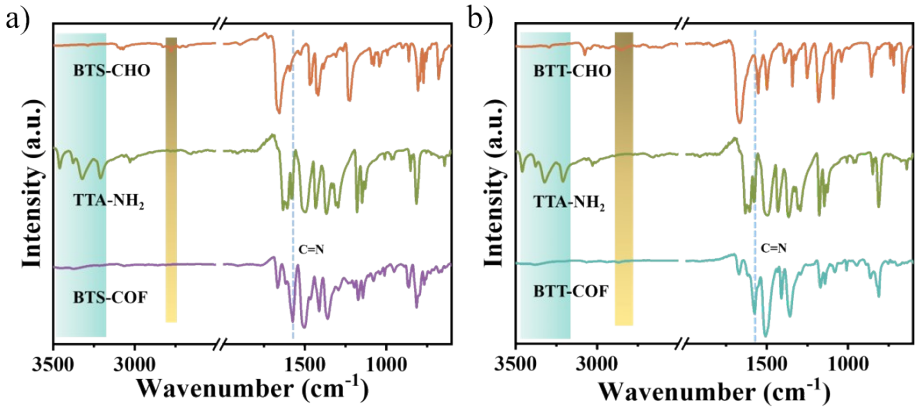

Fig. S4. a). FT-IR spectra of BTS-COF and monomers. b) FT-IR spectra of BTS-COF and monomers.

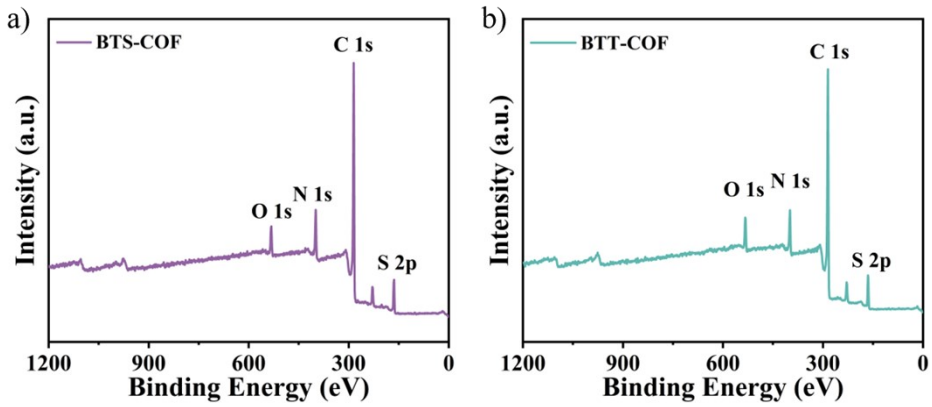

Fig. S5. a) XPS elemental spectra of BTS-COF. b) XPS elemental spectra of BTT-COF.

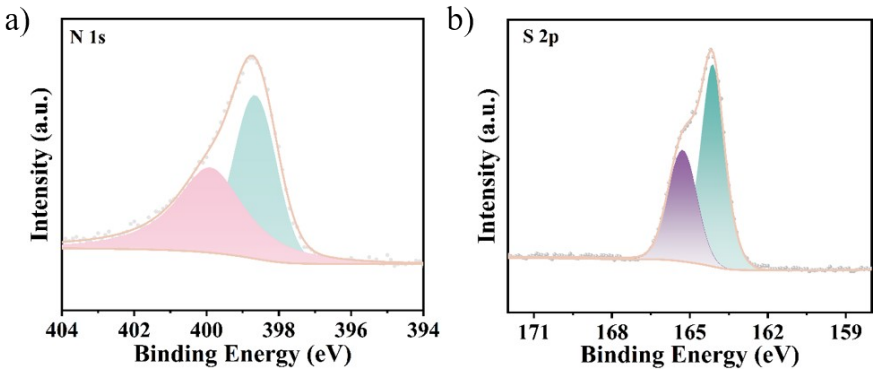

Fig. S6. High-resolution a) N 1s and d) S 2p X-ray photoelectron spectra of BTS-COF.

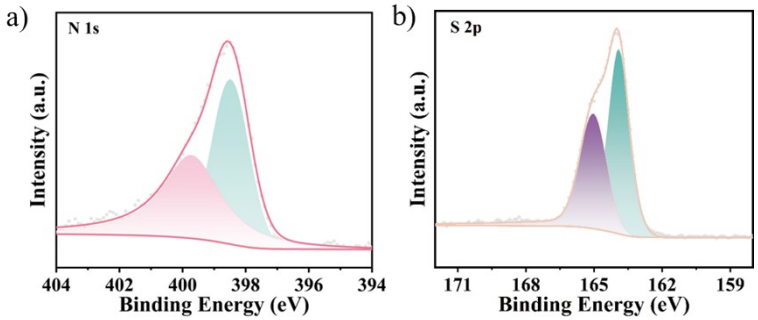

Fig. S7. High-resolution a) N 1s and d) S 2p X-ray photoelectron spectra of BTT-COF.

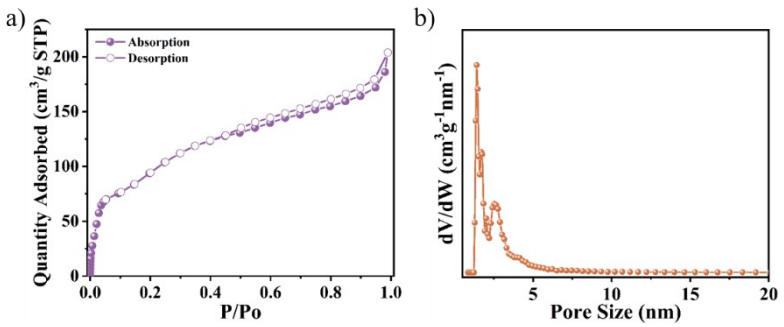

Fig. S8. a) N_2 sorption isotherm of BTS-COF. b) pore size distributions of BTS-COF.

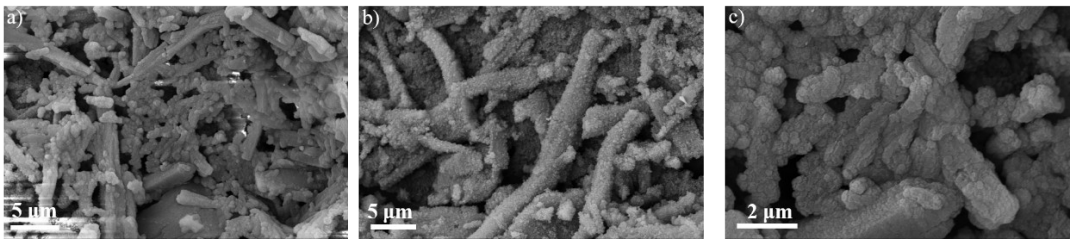

Fig. S9. SEM images of BTS-COF.

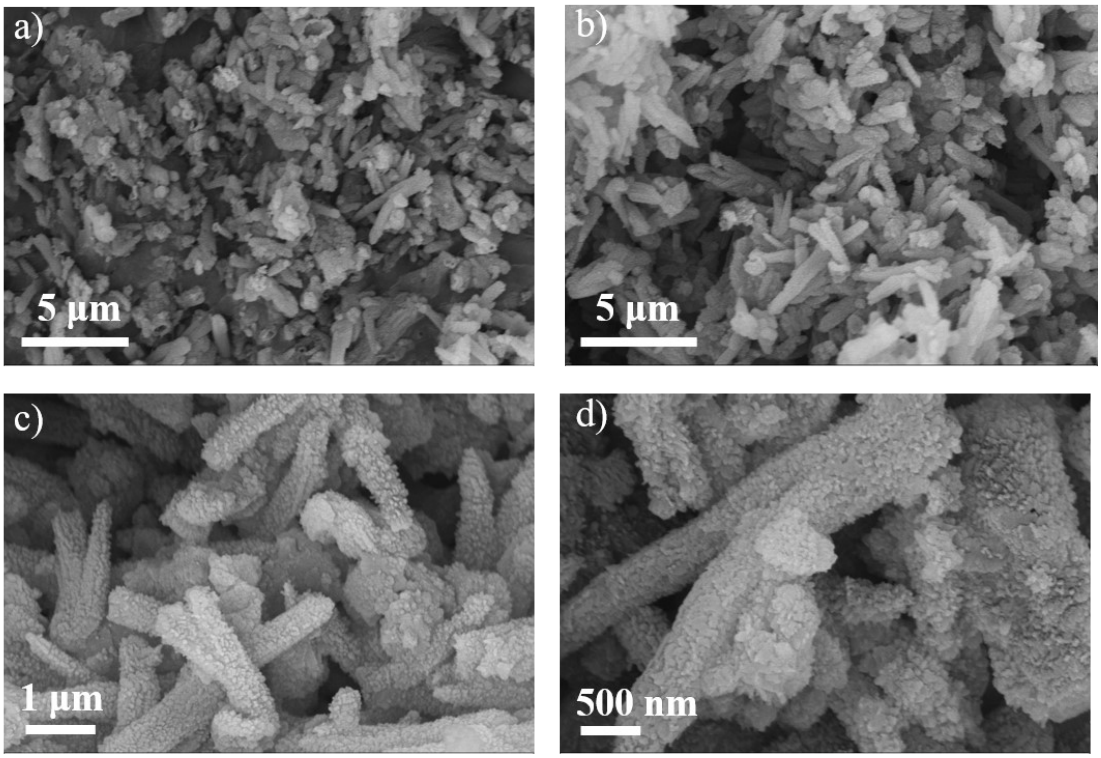

Fig. S10. SEM images of BTT-COF.

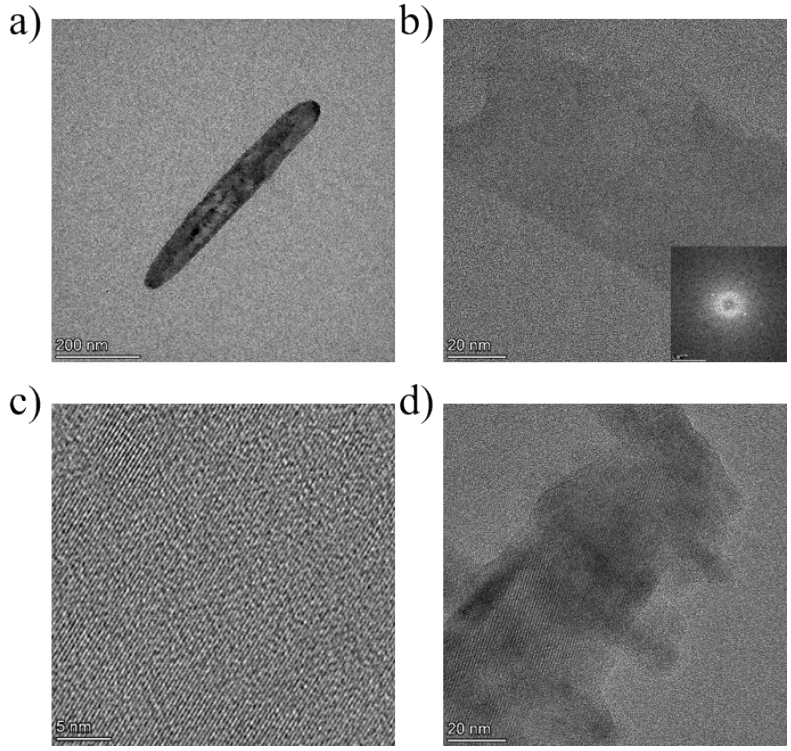

Fig. S11. TEM images of BTS-COF.

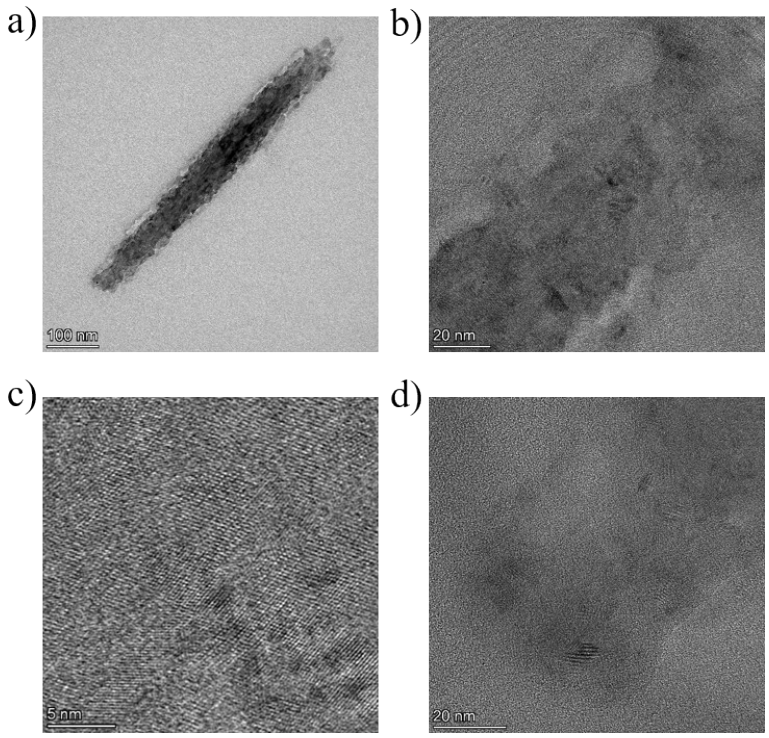

Fig. S12. TEM images of BTT-COF

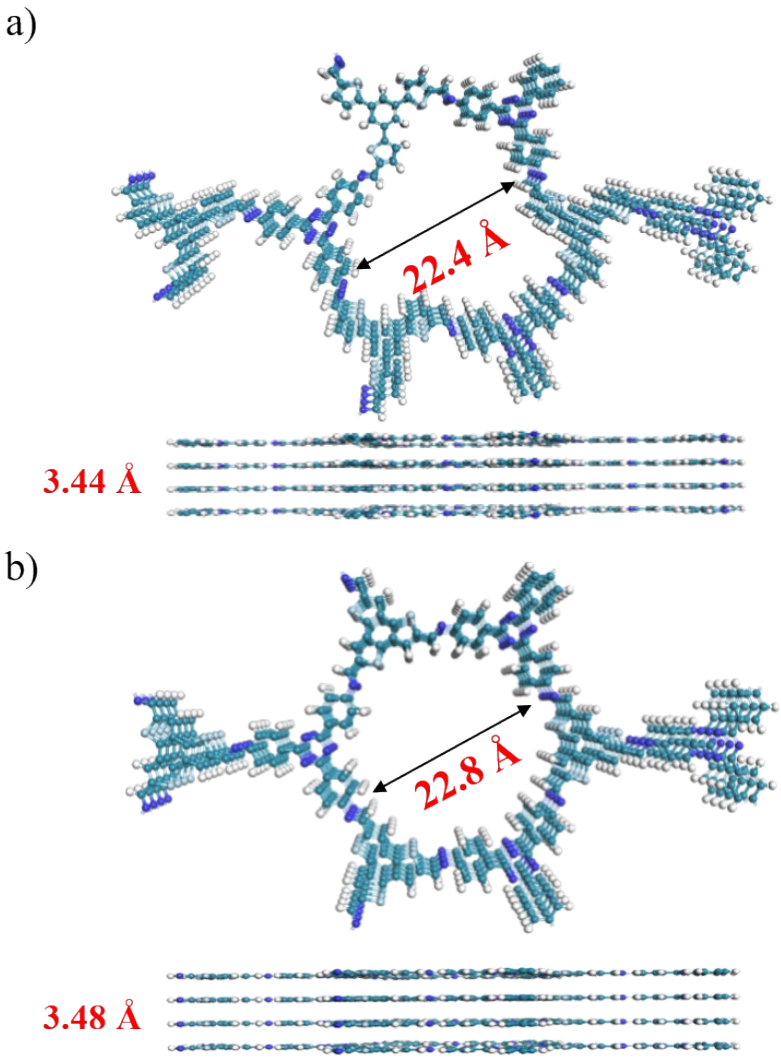

Fig. S13. a) Top and side views of the eclipsed stacking structure of BTS-COF. b) Top and side views of the eclipsed stacking structure of BTT-COF.

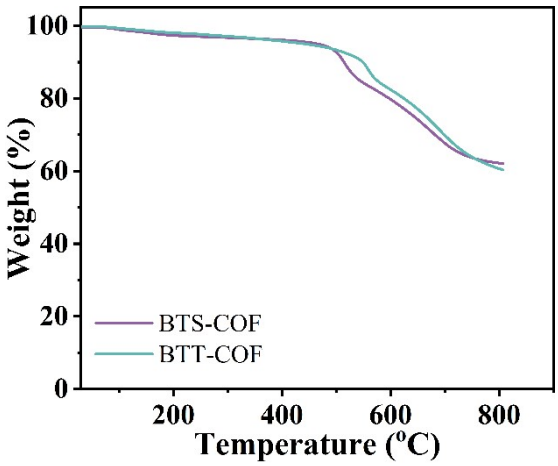

Fig. S14. TGA pattern of BTS-COF and BTT-COF.

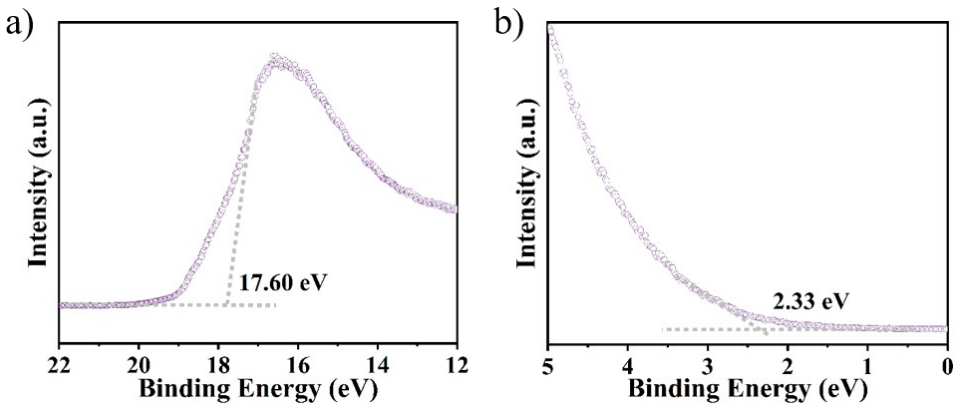

Fig. S15. UPS spectra of BTS-COF.

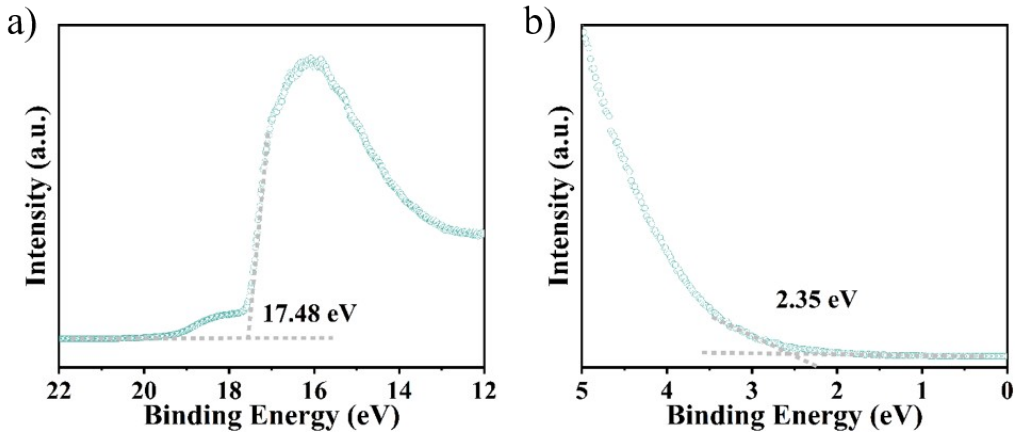

Fig. S16. UPS spectra of BTT-COF.

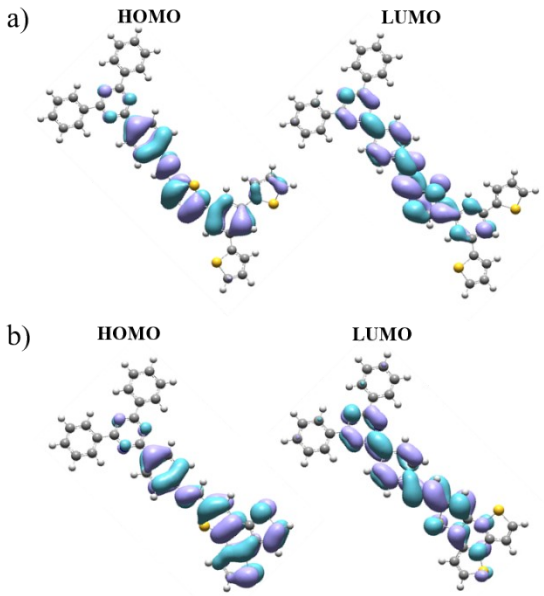

Fig. S17. Highest occupied molecular orbital and lowest unoccupied molecular orbital distribution of (a) BTS-COF and (b) BTT-COF.

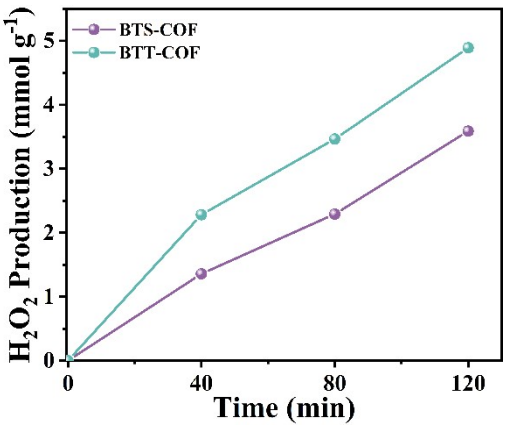

Fig. S18. Photocatalytic performance of BTS-COF and BTT-COF under add ethanol.

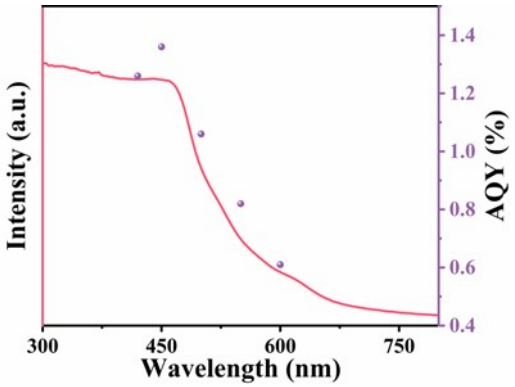

Fig.S19. AQY of BTT-COF under different monochromatic light conditions.

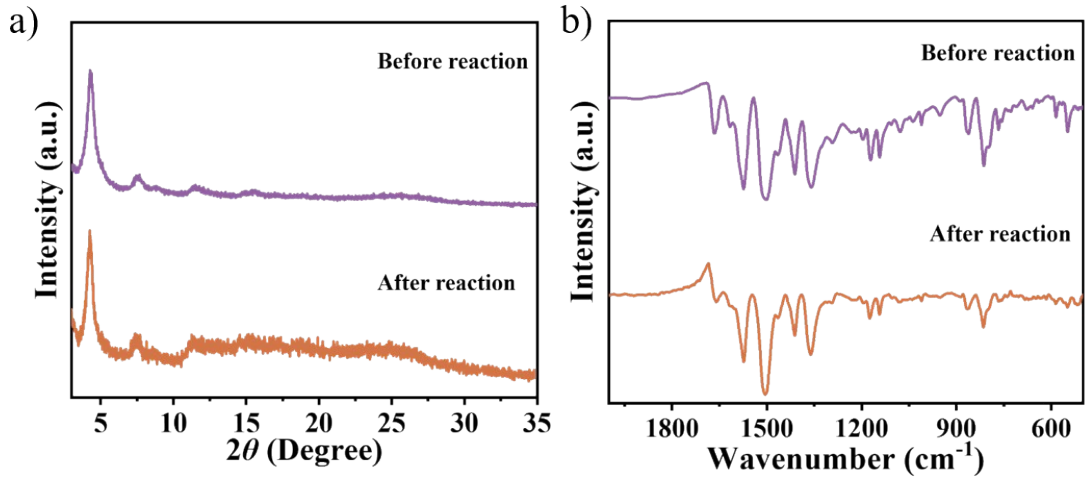

Fig. S20. a) PXRD patterns and b) FT-IR spectra of BTS-COF before and after cycling experiments.

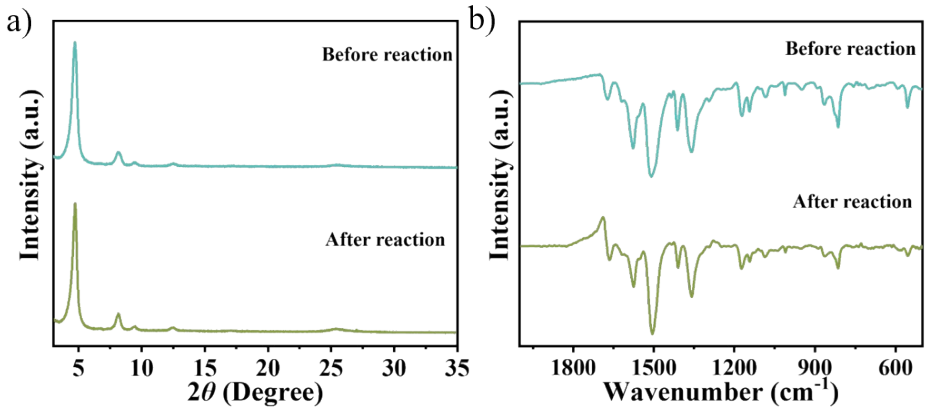

Fig. S21. a) PXRD patterns and b) FT-IR spectra of BTT-COF before and after cycling experiments.

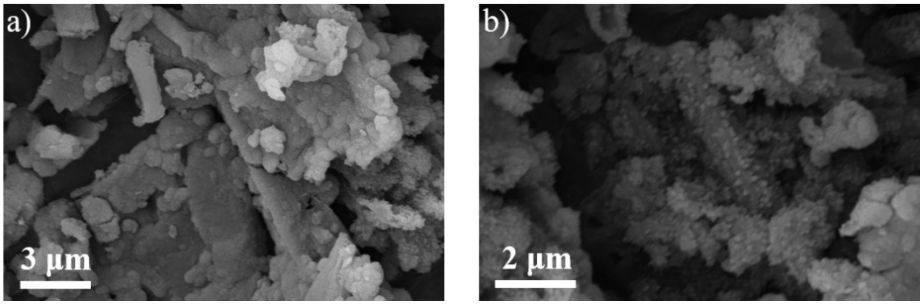

Fig. S22. SEM images of BTS-COF after cycling experiments.

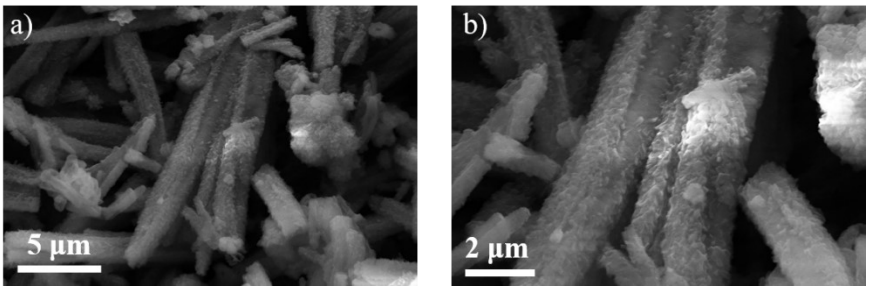

Fig. S23. SEM images of BTT-COF after cycling experiments.

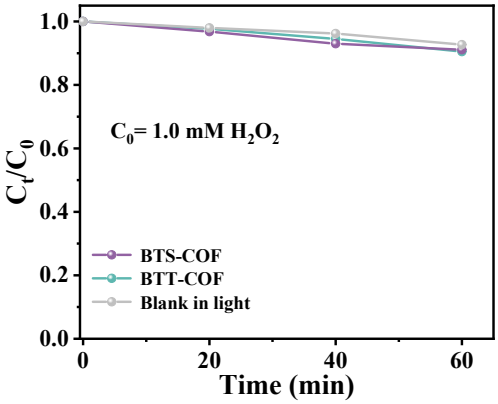

Fig. S24. Decomposition of H_2O_2 over BTS-COF and BTT-COF under N_2 atmosphere (λ>420 nm; 10 mg catalyst in 50 mL 1.0 mM H_2O_2 solution).

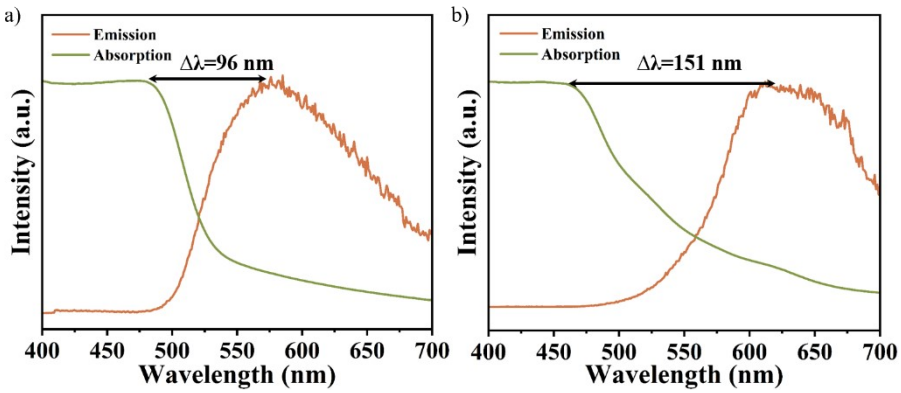

Fig. S25. Normalized absorption and emission spectra of a) BTS-COF and b) BTT-COF in solid state at 25 °C.

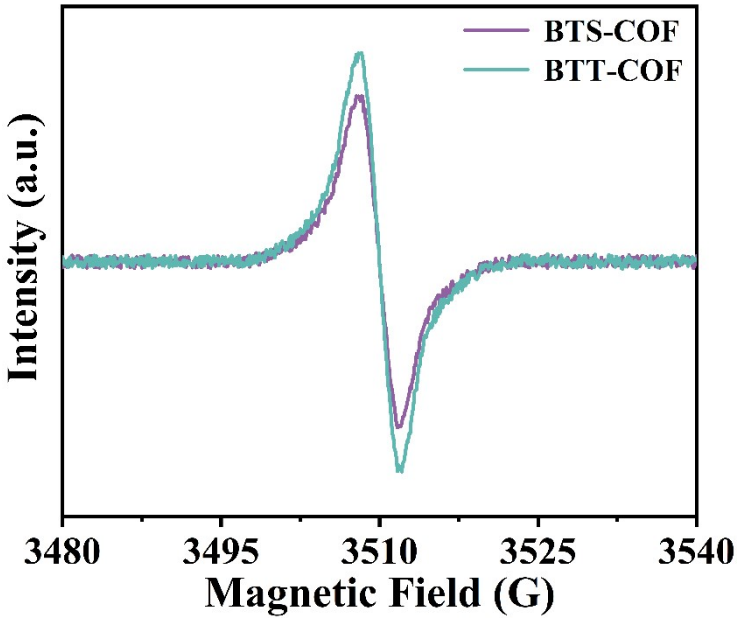

Fig. S26. EPR spectra of BTS-COF and BTT-COF under visible light irradiation.

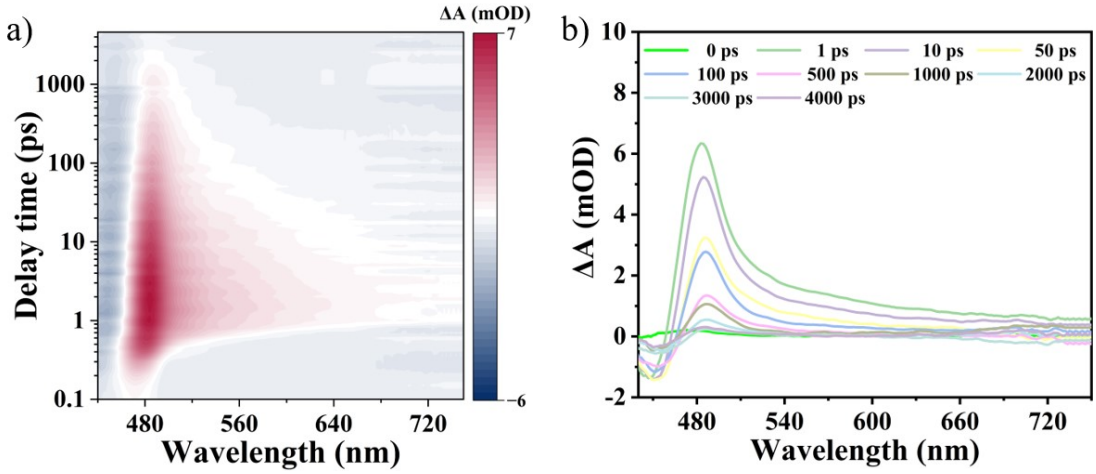

Fig. S27. (a) 2D fs-TA spectra mapping of BTS-COF. (b) Transient fs-TA spectra of BTS-COF

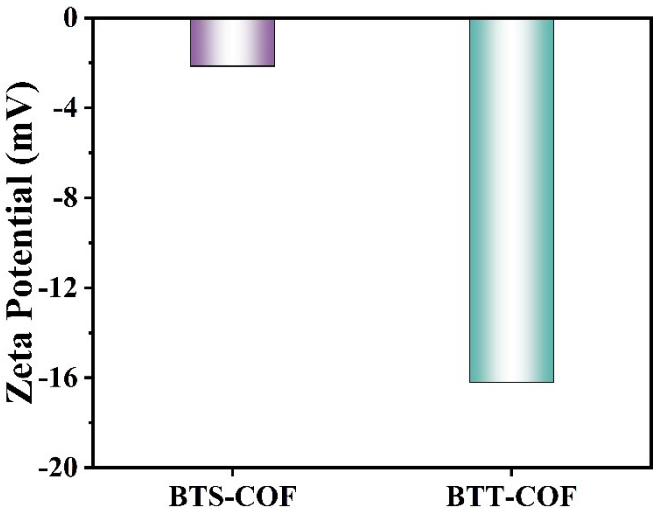

Fig. S28. Inter Zeta potential of BTS-COF and BTT-COF.

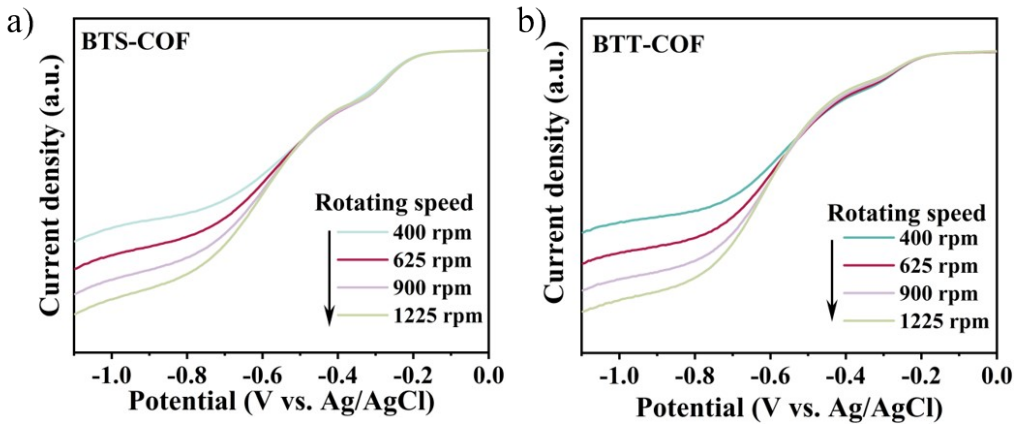

Fig. S29. LSV curves of (a) BTS-COF and (b) BTT-COF measured on RDE at different rotating speeds.

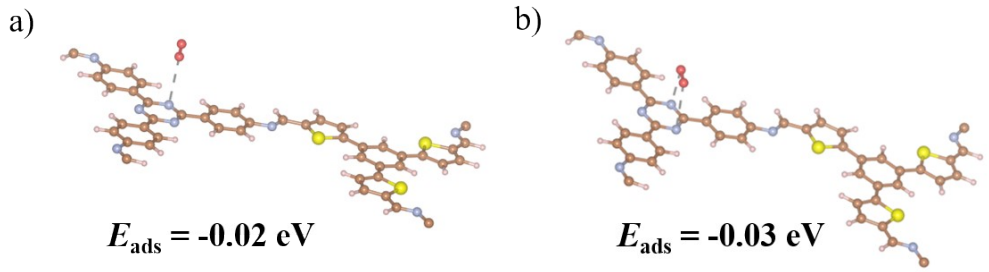

Fig. S30. Adsorption energy of oxygen on BTS-COF using different adsorption forms. a) Pauling-type. b) Yeager-type.

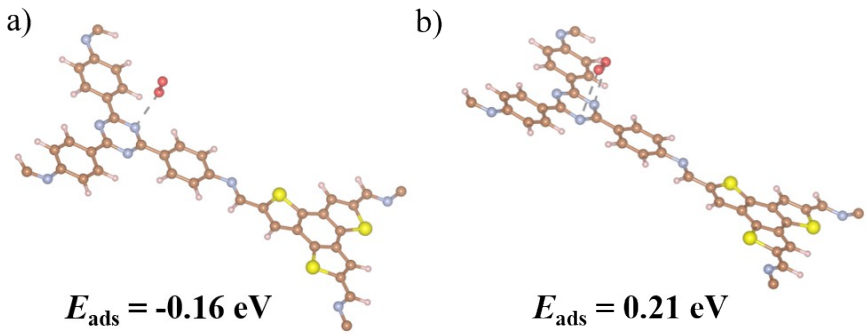

Fig. S31. Adsorption energy of oxygen on BTT-COF using different adsorption forms. a) Pauling-type. b) Yeager-type.

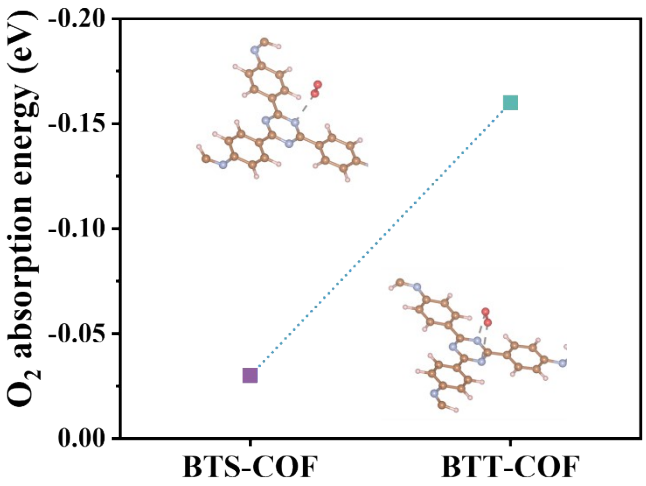

Fig. S32. The adsorption energy of O_2 on optimum site of BTS-COF and BTT-COF.

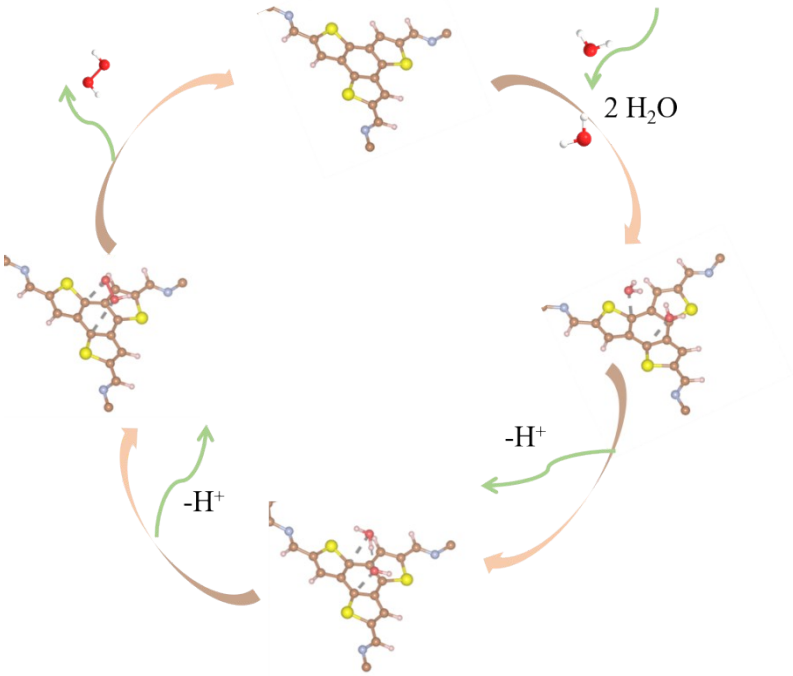

Fig. S33. Key steps of $2e^-$ WOR pathways of H_2O_2 production by BTT-COF.

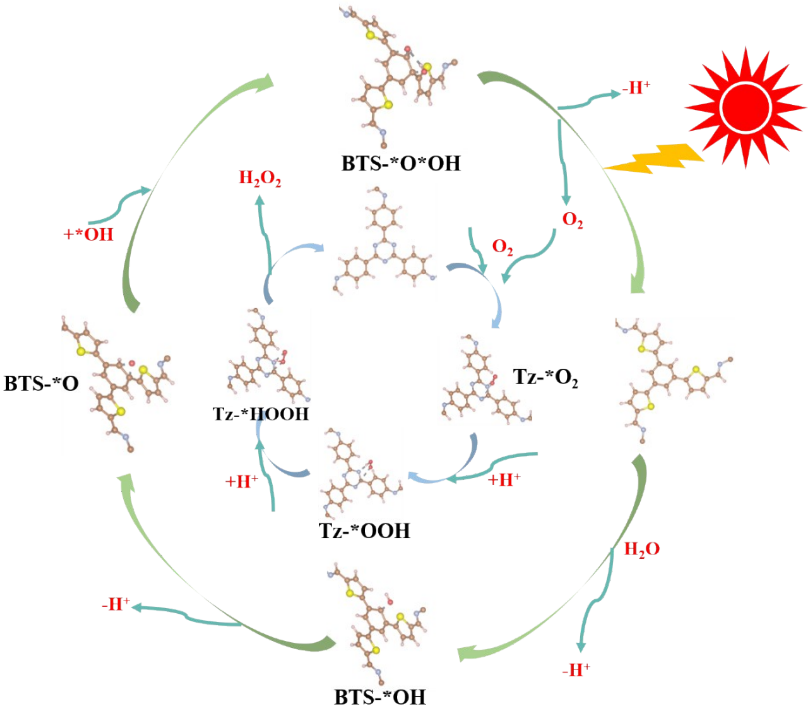

Fig. S34. Key steps of $2e^-$ WOR and $2e^-$ ORR pathways of H_2O_2 production by BTS-COF.

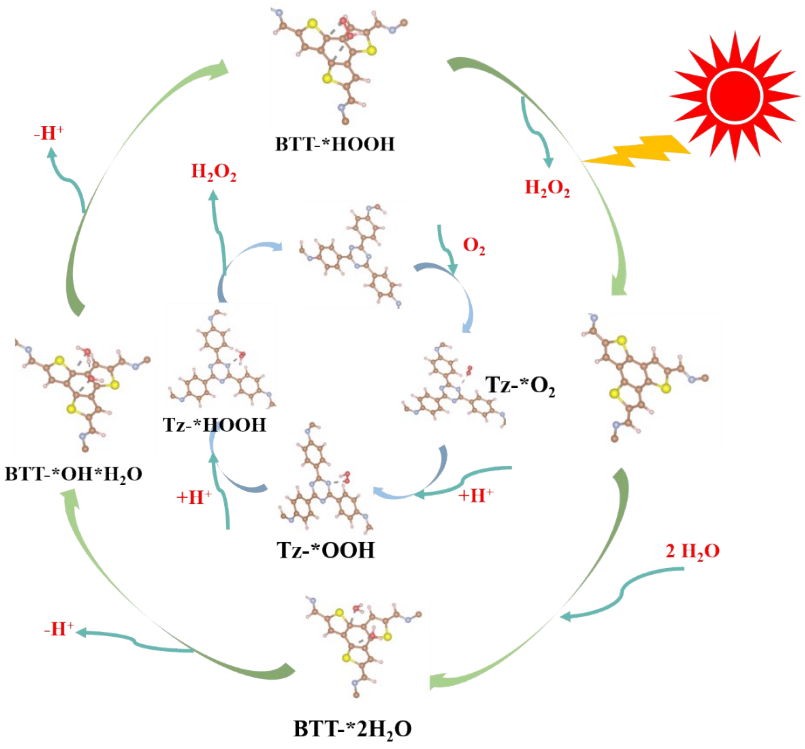

Fig. S35. Key steps of $2e^-$ WOR and $2e^-$ ORR pathways of H_2O_2 production by BTT-COF

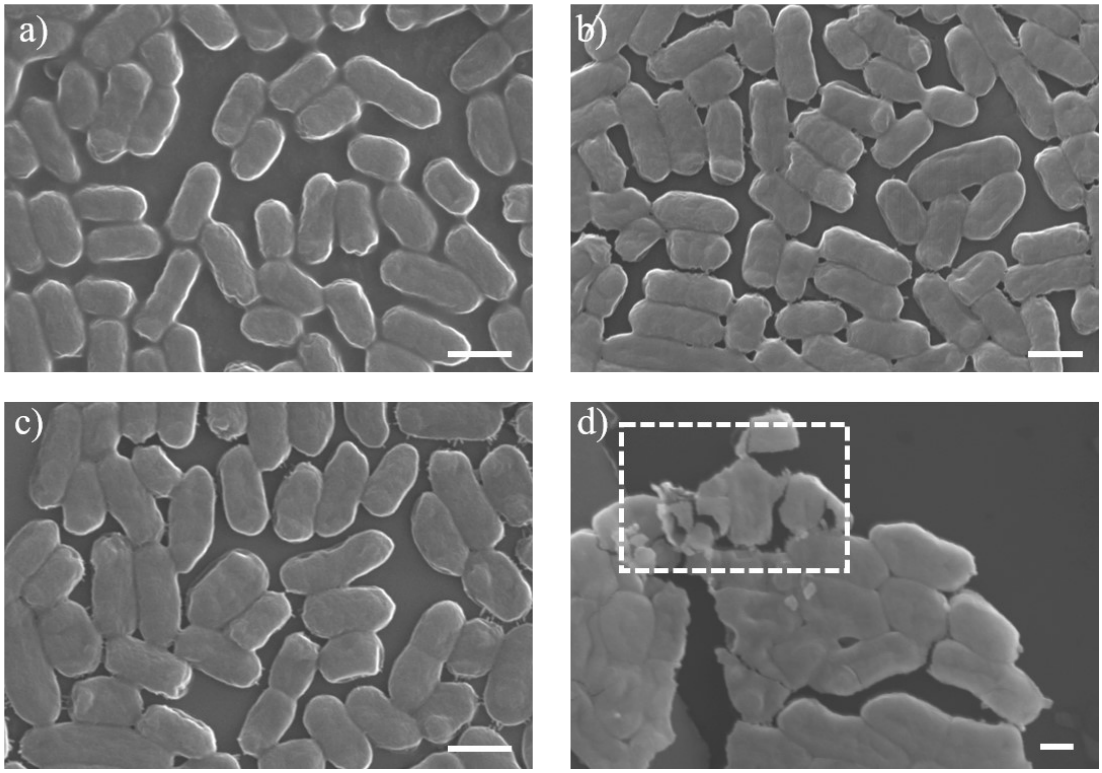

Fig. S36. SEM images of E. coli under different conditions. a) PBS + bacteria. b) PBS + bacteria + light. c) PBS + bacteria + COF. d) PBS + bacteria + COF + light. Scale bar: 1 μm.

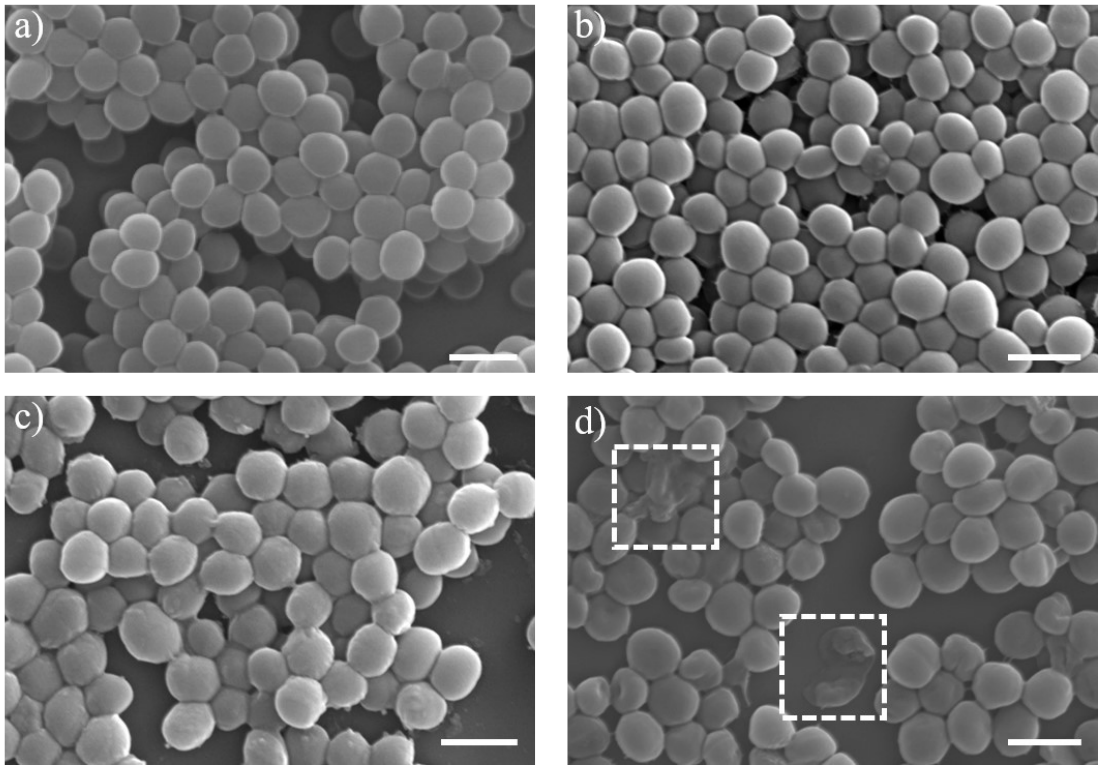

Fig. S37. SEM images of *S. au* under different conditions. a) PBS + bacteria. b) PBS + bacteria + light. c) PBS + bacteria + COF. d) PBS + bacteria + COF + light. Scale bar: 1 μm.

Table S1. Atomic parameters for slipped-parallel stacking model of the BTS-COF.

BTS-COF a = b = 23.95 Å, c = 3.44 Å, α = β = 90° and γ = 120°					
Atom	**Wyck**	**Site**	**x/a**	**y/b**	**z/c**
N1	3k	m	0.44808	0.00148	-0.5
C2	3k	m	0.42165	0.93331	-0.5
C3	3k	m	0.35511	0.88921	-0.5
C4	3k	m	1/3	0.82312	-0.5
C5	3k	m	0.37704	0.80045	-0.5
C6	3k	m	0.44338	0.84498	-0.5
C7	3k	m	0.46523	0.91072	-0.5
C8	3k	m	0.35426	0.73089	-0.5
N9	3k	m	0.29032	11/16	-0.5
C10	3k	m	0.64631	0.54203	-0.5
C11	3k	m	0.61579	0.58164	-0.5
S12	3k	m	0.60111	0.46008	-0.5
C13	3k	m	0.67057	0.4564	-0.5
C14	3k	m	0.72582	0.51692	-0.5
C15	3k	m	0.71169	0.5658	-0.5
C16	3k	m	0.669	0.39346	-0.5
C17	3k	m	0.6096	0.33548	-0.5
H18	3k	m	0.32007	0.90502	-0.5
H19	3k	m	0.28157	0.7899	-0.5
H20	3k	m	0.47858	0.82922	-0.5
H21	3k	m	0.51659	0.94448	-0.5
H22	3k	m	0.64484	0.63361	-0.5
H23	3k	m	0.77484	0.52633	-0.5
H24	3k	m	0.74761	0.61652	-0.5
H25	3k	m	0.56552	0.33704	-0.5

Table S2. Atomic parameters for slipped-parallel stacking model of the BTT-COF.

BTT-COF a = b = 22.05 Å, c = 3.48 Å, α = β = 90° and γ = 120°					
Atom	**Wyck**	**Site**	**x/a**	**y/b**	**z/c**
N1	3k	m	0.5036	0.0363	-0.5
C2	3k	m	0.47168	0.96167	-0.5
C3	3k	m	0.39859	0.92253	-0.5
C4	3k	m	0.3642	0.84967	-0.5
C5	3k	m	0.40276	0.81473	-0.5
C6	3k	m	0.47621	0.85402	-0.5
C7	3k	m	0.51053	0.92687	-0.5
C8	3k	m	0.36666	0.73777	-0.5
N9	3k	m	0.29578	0.69981	-0.5
H10	3k	m	0.36818	0.94878	-0.5
H11	3k	m	0.3075	0.82089	-0.5
H12	3k	m	0.50739	0.82858	-0.5
H13	3k	m	0.56702	0.95474	-0.5
C14	3k	m	0.91862	0.48862	-0.5
C15	3k	m	0.84425	7 月 16 日	-0.5
C16	3k	m	0.7933	0.45587	-0.5
C17	3k	m	0.72834	0.39753	-0.5
C18	3k	m	0.73132	0.33626	-0.5
S19	3k	m	0.81384	0.34835	-0.5
H20	3k	m	0.93427	0.54349	-0.5
H21	3k	m	0.80348	0.50927	-0.5

Table S3. Photocatalytic activity of representative COF-based photocatalysts.

Photocatalysts	**Light source**	**Reaction solution**	**H_2O_2 yield (μmol g^{-1} h^{-1})**
BTS-COF	λ > 420 nm	H_2O : EtOH	1786
BTT-COF	λ > 420 nm	H_2O : EtOH	2904
PBBT-COF[2]	λ > 420 nm	H_2O	1564
TfpBpy-COF[3]	λ > 420 nm	H_2O	695
FS-OHOHMe-COF[4]	λ > 420 nm	H_2O:BA (9:1)	1458
TAPD-$(Me)_2$-COF[5]	λ > 420 nm	H_2O : EtOH	97
PyDa-COF[6]	λ > 420 nm	H_2O : EtOH	412.7
TTF-BT-COF[7]	λ > 420 nm	H_2O	2760
TpAQ-COF-12[8]	λ > 420 nm	H_2O	420
CTF-BDDBN[9]	λ > 420 nm	H_2O	97.2
Cu_2-BT-COF[10]	λ > 420 nm	H_2O : FAA	1168
CTF-NS-5BT[11]	λ > 420 nm	H_2O	1630
EBA-COF[12]	λ > 420 nm	H_2O : EtOH	1830
COF-2CN[13]	λ > 420 nm	H_2O	1601
HITMS-COF-21H^+[14]	λ > 420 nm	H_2O : EtOH	1957
4PE-NS-COF[15]	λ > 420 nm	H_2O	1574
TiO_2/BTTA[16]	λ > 420 nm	H_2O : FAL	740
$CsPbBr_3$/CTFS[17]	λ > 420 nm	H_2O	296.2
CuBr-dptz[18]	λ > 420 nm	H_2O	1874
COF-NUST-16[19]	λ > 420 nm	H_2O : EtOH	1081
PMCR-1[20]	λ > 420 nm	H_2O	1445
N_0-COF[21]	λ > 420 nm	H_2O	1570
TiCOF-spn[22]	λ > 420 nm	H_2O : EtOH	489.9
HEP-TAPT-COF[23]	λ > 420 nm	H_2O	1750
CQD-CTFs[24]	λ > 420 nm	H_2O	1036
1H-COF[25]	λ > 420 nm	H_2O : IPA	1483
CDs@CTFs[26]	λ > 420 nm	H_2O	535.4
TF_{30}-COF[27]	λ > 420 nm	H_2O : EtOH	1739
CHF-DPDA[28]	λ > 420 nm	H_2O	1725
PBBT-COF[29]	λ > 420 nm	H_2O	1563

Table S4. Time-resolved photoluminescence fitting data for BTS-COF and BTT-COF

	BTS-COF		BTT-COF	
	Value (ns)	Rel.%	Value (ns)	Rel.%
τ_1	1.02	37.3	0.45	15.2
τ_2	0.17	62.7	1.44	84.8
A_1	186.88		749.01	
A_2	1886.99		1299.72	
τ_{ave}	0.48		1.29	

Reference

(1) Wei, H.; Ning, J.; Cao, X.; Li, X.; Hao, L. Benzotrithiophene-Based Covalent Organic Frameworks: Construction and Structure Transformation under Ionothermal Condition. *J. Am. Chem. Soc.* **2018**, *140* (37), 11618-11622.
(2) Li, B.; Chen, J.; Wang, K.; Qi, D.; Wang, T.; Jiang, J. Ethynyl-Linked Donor–Acceptor Covalent Organic Framework for Highly Efficient Photocatalytic H_2O_2 Production. *Adv. Energy Mater.* **2025**, *15* (18), 2404497.
(3) Kou, M.; Wang, Y.; Xu, Y.; Ye, L.; Huang, Y.; Jia, B.; Li, H.; Ren, J.; Deng, Y.; Chen, J.; et al. Molecularly Engineered Covalent Organic Frameworks for Hydrogen Peroxide Photosynthesis. *Angew. Chem. Int. Ed.* **2022**, *61* (19), e202200413.
(4) Shu, C.; Yang, X.; Liu, L.; Hu, X.; Sun, R.; Yang, X.; Cooper, A. I.; Tan, B.; Wang, X. Mixed-Linker Strategy for the Construction of Sulfone-Containing D–A–A Covalent Organic Frameworks for Efficient Photocatalytic Hydrogen Peroxide Production. *Angew. Chem. Int. Ed.* **2024**, *63* (22), e202403926.
(5) Krishnaraj, C.; Sekhar Jena, H.; Bourda, L.; Laemont, A.; Pachfule, P.; Roeser, J.; Chandran, C. V.; Borgmans, S.; Rogge, S. M. J.; Leus, K.; et al. Strongly Reducing (Diarylamino)benzene-Based Covalent Organic Framework for Metal-Free Visible Light Photocatalytic H2O2 Generation. *J. Am. Chem. Soc.* **2020**, *142* (47), 20107-20116.
(6) Sun, J.; Sekhar Jena, H.; Krishnaraj, C.; Singh Rawat, K.; Abednatanzi, S.; Chakraborty, J.; Laemont, A.; Liu, W.; Chen, H.; Liu, Y.-Y.; et al. Pyrene-Based Covalent Organic Frameworks for Photocatalytic Hydrogen Peroxide Production. *Angew. Chem. Int. Ed* **2023**, *62* (19), e202216719.
(7) Chang, J.-N.; Li, Q.; Shi, J.-W.; Zhang, M.; Zhang, L.; Li, S.; Chen, Y.; Li, S.-L.; Lan, Y.-Q. Oxidation-Reduction Molecular Junction Covalent Organic Frameworks for Full Reaction Photosynthesis of H_2O_2. *Angew. Chem. Int. Ed.* **2023**, *62* (9), e202218868.
(8) Zhang, X.; Zhang, J.; Miao, J.; Wen, X.; Chen, C.; Zhou, B.; Long, M. Keto-enamine-based covalent organic framework with controllable anthraquinone moieties for superior H2O2 photosynthesis from O2 and water. *Chem. Eng. J* **2023**, *466*, 143085.
(9) Chen, L.; Wang, L.; Wan, Y.; Zhang, Y.; Qi, Z.; Wu, X.; Xu, H. Acetylene and Diacetylene Functionalized Covalent Triazine Frameworks as Metal-Free Photocatalysts for Hydrogen Peroxide Production: A New Two-Electron Water Oxidation Pathway. *Adv. Mater.* **2020**, *32* (2), 1904433.
(10) Chang, J.-N.; Shi, J.-W.; Li, Q.; Li, S.; Wang, Y.-R.; Chen, Y.; Yu, F.; Li, S.-L.; Lan, Y.-Q. Regulation of Redox Molecular Junctions in Covalent Organic Frameworks for H2O2 Photosynthesis Coupled with Biomass Valorization. *Angew. Chem. Int. Ed.* **2023**, *62* (31), e202303606.
(11) Yu, X.; Viengkeo, B.; He, Q.; Zhao, X.; Huang, Q.; Li, P.; Huang, W.; Li, Y. Electronic Tuning of Covalent Triazine Framework Nanoshells for Highly Efficient Photocatalytic H_2O_2 Production. *Adv. Sustainable Syst.* **2021**, *5* (10), 2100184.
(12) Zhai, L.; Xie, Z.; Cui, C.-X.; Yang, X.; Xu, Q.; Ke, X.; Liu, M.; Qu, L.-B.; Chen, X.; Mi, L. Constructing Synergistic Triazine and Acetylene Cores in Fully Conjugated Covalent Organic Frameworks for Cascade Photocatalytic H_2O_2 Production. *Chem. Mater.* **2022**, *34* (11), 5232-5240.
(13) Hou, Y.; Zhou, P.; Liu, F.; Lu, Y.; Tan, H.; Li, Z.; Tong, M.; Ni, J. Efficient Photosynthesis of Hydrogen Peroxide by Cyano-Containing Covalent Organic Frameworks from Water, Air and Sunlight. *Angew. Chem. Int. Ed.* **2024**, *63* (6), e202318562.
(14) Wang, L.; Han, C.; Gao, S.; Jiang, J.-X.; Zhang, Y. Covalent Organic Frameworks Enhance Photocatalytic Hydrogen Peroxide Production through Synergistic Effects. *ACS Catal.* **2025**, *15* (7), 5683-5693.
(15) Deng, M.; Sun, J.; Laemont, A.; Liu, C.; Wang, L.; Bourda, L.; Chakraborty, J.; Van Hecke, K.;

Morent, R.; De Geyter, N.; et al. Extending the π-conjugation system of covalent organic frameworks for more efficient photocatalytic H_2O_2 production. *Green Chem.* **2023**, *25* (8), 3069-3076.
(16) Yang, Y.; Liu, J.; Gu, M.; Cheng, B.; Wang, L.; Yu, J. Bifunctional TiO2/COF S-scheme photocatalyst with enhanced H_2O_2 production and furoic acid synthesis mechanism. *Appl. Catal. B* **2023**, *333*, 122780.
(17) Zheng, Y.; Gao, T.; Chen, S.; Ferguson, C. T. J.; Zhang, K. A. I.; Fang, F.; Shen, Y.; Khan, N. A.; Wang, L.; Ye, L. CsPbBr3 quantum dots-decorated porous covalent triazine frameworks nanocomposites for enhanced solar-driven H_2O_2 production. *Compos. Commun.* **2022**, *36*, 101390.
(18) Zhang, J.; Lei, H.; Li, Z.; Jiang, F.; Chen, L.; Hong, M. Halogen-Modulated 2D Coordination Polymers for Efficient Hydrogen Peroxide Photosynthesis under Air and Pure Water Conditions. *Angew. Chem. Int. Ed.* **2024**, *63* (3), e202316998.
(19) Wu, M.; Shan, Z.; Wang, J.; Liu, T.; Zhang, G. Three-dimensional covalent organic framework with tty topology for enhanced photocatalytic hydrogen peroxide production. *Chem. Eng. J.* **2023**, *454*, 140121.
(20) Das, P.; Roeser, J.; Thomas, A. Solar Light Driven H_2O_2 Production and Selective Oxidations Using a Covalent Organic Framework Photocatalyst Prepared by a Multicomponent Reaction. *Angew. Chem. Int. Ed.* **2023**, *62* (29), e202304349.
(21) Chai, S.; Chen, X.; Zhang, X.; Fang, Y.; Sprick, R. S.; Chen, X. Rational design of covalent organic frameworks for efficient photocatalytic hydrogen peroxide production. *Environ. Sci.:Nano* **2022**, *9* (7), 2464-2469.
(22) Han, W.-K.; Lu, H.-S.; Fu, J.-X.; Liu, X.; Zhu, X.; Yan, X.; Zhang, J.; Jiang, Y.; Dong, H.; Gu, Z.-G. Targeted construction of a three-dimensional metal covalent organic framework with spn topology for photocatalytic hydrogen peroxide production. *Chem. Eng. J.* **2022**, *449*, 137802.
(23) Chen, D.; Chen, W.; Zhang, G.; Li, S.; Chen, W.; Xing, G.; Chen, L. N-Rich 2D Heptazine Covalent Organic Frameworks as Efficient Metal-Free Photocatalysts. *ACS Catal.* **2022**, *12* (1), 616-623.
(24) Yang, Y.; Guo, Q.; Li, Q.; Guo, L.; Chu, H.; Liao, L.; Wang, X.; Li, Z.; Zhou, W. Carbon Quantum Dots Confined into Covalent Triazine Frameworks for Efficient Overall Photocatalytic H2O2 Production. *Adv. Funct. Mater.* **2024**, *34* (29), 2400612.
(25) Hu, H.; Tao, Y.; Wang, D.; Li, C.; Jiang, Q.; Shi, Y.; Wang, J.; Qin, J.; Zhou, S.; Kong, Y. Rational modification of hydroxy-functionalized covalent organic frameworks for enhanced photocatalytic hydrogen peroxide evolution. *J. Colloid Interface Sci.* **2023**, *629*, 750-762.
(26) Ren, W.; Chang, Q.; Li, N.; Yang, J.; Hu, S. Carbon dots-modulated covalent triazine frameworks with exceptionally rapid hydrogen peroxide production in water. *Chem. Eng. J.* **2023**, *451*, 139035.
(27) Wang, H.; Yang, C.; Chen, F.; Zheng, G.; Han, Q. A Crystalline Partially Fluorinated Triazine Covalent Organic Framework for Efficient Photosynthesis of Hydrogen Peroxide. *Angew. Chem. Int. Ed.* **2022**, *61* (19), e202202328.
(28) Cheng, H.; Lv, H.; Cheng, J.; Wang, L.; Wu, X.; Xu, H. Rational Design of Covalent Heptazine Frameworks with Spatially Separated Redox Centers for High-Efficiency Photocatalytic Hydrogen Peroxide Production. *Adv. Mater.* **2022**, *34* (7), 2107480.
(29) Li, B.; Chen, J.; Wang, K.; Qi, D.; Wang, T.; Jiang, J. Ethynyl-Linked Donor–Acceptor Covalent Organic Framework for Highly Efficient Photocatalytic H_2O_2 Production. *Adv. Energy Mater.* **2025**, *15*

(18), 2404497..